Fracture and fragmentation of blast-loaded laminated glass: An experimental and numerical study

Karoline Osnes*,a,b, Jens Kristian Holmen[a], Odd Sture Hopperstad[a,b], Tore Børvik[a,b]

[a] Structural Impact Laboratory (SIMLab), Department of Structural Engineering, Norwegian University of Science and Technology (NTNU), Trondheim, NO-7491, Norway
[b] Centre for Advanced Structural Analysis (CASA), NTNU, NO-7491, Trondheim, Norway

ABSTRACT

In this study, we use the explicit finite element method in combination with higher order elements and 3D node splitting to simulate fracture and fragmentation of blast-loaded laminated glass. Node splitting is a modelling technique where elements are separated instead of being eroded when a fracture criterion is reached. The resulting FE simulations are thus capable of describing behaviours such as fragmentation without loss of mass or momentum, fine cracking of the glass plates, and delamination and separation between the glass and the polymer interlayer. The simulations are compared to blast experiments conducted in a shock tube. In total, 15 laminated glass specimens (consisting of annealed float glass plates and PVB) were tested at five different pressure levels. The time and position of fracture initiation in the glass plates varied, which in turn resulted in varying post-fracture behaviour within the different pressure levels. The simulations were in good agreement with the blast tests, revealing the potential of the selected numerical method. Additional simulations of monolithic (i.e., non-laminated) glass plates were conducted and compared to experiments that were presented in an earlier study. Again, these simulations displayed a highly comparable response to the experiments, and were able to describe crack branching, formation of large glass splinters and free-flying fragments.

1. Introduction

In recent years, extreme conditions such as blast and impact loading have become important aspects in structural design. Window systems are generally considered the most vulnerable part of a structural facade, as they mainly consist of annealed float glass. Glass is a brittle material, and when it fails, it will break in a sudden manner into numerous sharp fragments. Laminated glass is often used as an alternative to increase the safety of window systems in the event of an explosion or an impact, and consists of two or more glass plates bonded together with a polymer interlayer, usually polyvinyl butural (PVB). The polymer interlayer retains broken glass fragments and increases the loading resistance of the window system. If a flexible polymer is used (e.g., PVB), deformation of the interlayer absorbs energy, which in turn reduces the energy transmitted to the rest of the structure. The post-fracture behaviour of laminated glass subjected to blast loading is a complex process and has been a topic of research for several years. The open literature includes many experimental studies on blast-loaded laminated glass, both field tests [1–4] and shock tube tests [5–7]. In a recent study by Osnes et al. [8], the combined effect of fragment impact and blast loading on laminated glass was studied experimentally. A number of researchers

have used finite element (FE) simulations with the aim of recreating the mechanical behaviour observed in the experiments. Among them, Larcher et al. [1] studied the behaviour of a solid element model, a shell element model and a smeared model, and concluded that the solid element model gave the most accurate result. Hooper et al. [2] developed a shell element model where the stiffness of the glass layer was set to zero when it fractured. The technique gave comparable results to experiments. Zhang et al. [4] studied the failure mechanisms of laminated window systems through FE simulations, and found that the boundary conditions dominate the behaviour. The study emphasised the importance of accurate modelling of the window frame. Pelfrene et al. [7] developed a detailed FE model of a blast-loaded laminated glass, and investigated the possibility of delamination between the glass and the PVB. The numerical model was able to capture many aspects of the post-fracture behaviour. However, the authors emphasised the need of a very fine mesh to model the fracture and delamination processes accurately when using element erosion. Another study of importance is the experimental and numerical investigation of pre-cracked laminated glass specimens under tensile loading by Del Linz et al. [9]. The authors found that the delamination process in terms of delamination energy is dependent on the loading rate. Franz and Schneider [10] performed

---

similar experiments and showed that the delamination properties are strongly dependent on the adhesion level between the PVB and the glass. The delamination properties are also found to be dependent on the ambient temperature [11]. Other aspects to consider is the probabilistic fracture strength of glass, which arises from microscopic flaws located on the surface [12]. In a recent work by Osnes et al. [13], the strength of glass plates exposed to an arbitrary loading history was estimated by a stochastic strength model. The model utilises stress fields from FE simulations and performs virtual experiments on a large number of glass plates. The stochastic strength model is based on the work of Yankelevsky [14].

In the current study, we use the explicit finite element method combined with higher-order elements and node splitting in simulations of blast-loaded laminated glass specimens. Node splitting is an alternative to element erosion, in which elements are separated instead of deleted when a fracture criterion is reached. By employing node splitting, a number of obstacles associated with element erosion are avoided. To further demonstrate the use of the modelling techniques, we also run simulations of blast-loaded monolithic (i.e., non-laminated) glass plates. The simulations of both laminated and monolithic glass are compared to blast experiments performed in a shock tube [15]. A total of 15 laminated glass specimens (made from annealed float glass plates and PVB) were tested at five different pressure levels. The time and position of fracture initiation varied in the tests, which in turn resulted in varying post-fracture behaviour within the different pressure levels. The experiments on monolithic glass were presented in an earlier study by Osnes et al. [13]. In the FE simulations presented in this study, glass fracture takes place upon reaching a deterministic failure criterion. Since the fracture strength of glass is probabilistic, this is a simplification of the problem. However, as the main purpose of the numerical study is to investigate the applicability of the selected simulation method, this simplification is deemed justifiable, even if the stochastic fracture behaviour of glass should be considered in the design of laminated glass components.

2. Materials

2.1. Float glass

The laminated glass used in this study consists of clear soda-lime silica float glass, which has undergone an annealing process. This process results in glass plates with nearly no internal residual stresses. Float glass is a brittle material and has a linear elastic behaviour until it fails suddenly into sharp fragments. Fracture in glass typically initiates in microscopic flaws randomly located on the surface, which results in a highly stochastic fracture behaviour [13]. The flaws also cause glass plates to primarily fail in tension, since crack propagation is induced by mode I loading (i.e., opening of a flaw) [12]. Commonly used material parameters for float glass are presented in Table 1 [16]. The fracture toughness K_{IC} is the critical stress intensity factor for mode I loading. The value stated in the table is based on quasi-static tests by Wiederhorn [17]. It should, however, be noted that the fracture strength of glass is found to be strain-rate sensitive [18,19], which could affect the fracture toughness. The strain-rate dependency is believed to be caused by a type of stress-corrosion [20], i.e., a phenomenon driven by water vapour in the surroundings [21].

Table 1
Material parameters for soda-lime-silica glass.

Density ρ	Young's modulus E	Poisson's ratio ν	Fracture toughness K_{IC}
$2500 \, \text{kg/m}^3$	70000 MPa	0.2	$0.75 \, \text{MPa}\sqrt{\text{m}}$
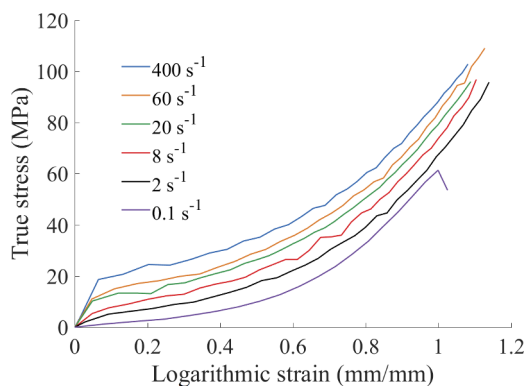
Fig. 1. Selected tensile tests on PVB performed by Hooper et al. [22] and Del Linz et al. [24]. The legend refers to the nominal strain rate.

2.2. Polyvinyl butyral (PVB)

The laminated glass used in this study includes an interlayer made from polyvinyl butyral (PVB). It is the most commonly used interlayer in laminated window glass, and is also frequently used as a component in automobile windshields [7]. PVB is a highly flexible material, and may undergo large strains before failure. Additionally, it exhibits temperature and strain-rate dependent nonlinear behaviour [22–24] with hardly any permanent deformation some time after loading [23]. PVB is usually considered to be nearly incompressible [1], and it has been reported that the failure strain of PVB decreases with increasing strain rate [23]. The viscoelastic response of PVB is illustrated in Fig. 1, which shows true stress-logarithmic strain curves from uniaxial tensile tests at different strain rates. It is seen that the curves from the high strain-rate tests include a point where the stiffness changes. This effect is not observed at low strain rates. The uniaxial tensile tests presented in Fig. 1 were performed on PVB dogbone specimens by Hooper et al. [22] and Del Linz et al. [24].

2.3. Laminated glass

Laminated glass consists of two or more glass plates bonded together with a polymer interlayer (usually PVB). The bonding is mainly a result of a process including heat and pressure in an autoclave. Compared to monolithic glass, laminated glass has several beneficial attributes. If the glass breaks, the glass fragments adhere to the polymer, resulting in a safer glass solution, especially against blast and impact loading. The interlayer also provides additional resistance by distributing forces over a larger area of the plate. A flexible interlayer, such as PVB, can also absorb energy during loading and in turn reduce the energy transmitted to the rest of the structure (e.g., building or automobile). The pre-fracture behaviour of laminated glass is relatively simple, with linear-elastic behaviour of the glass plates [1]. The interlayer transfers shear forces between the glass layers to a varying extent depending on the stiffness of the interlayer. After fracture of the glass plates, the behaviour is more complex. Delamination occurs between the glass and the interlayer around the cracks in the glass, which leads to stretching of the interlayer. A strong adhesion between the interlayer and glass might not be desirable as this can lead to stretching over a small area and tearing of the interlayer [7]. However, a sufficient adhesion level must be achieved to limit the amount of detaching glass fragments. The adhesion level is dependent on the autoclave process and the applied polymer type.

3. Experimental study

3.1. Blast loading

In the event of a chemical explosion, a shock wave is generated and followed by a series of pressure waves, thus forming a blast wave. The blast pressure, i.e., the pressure profile of the blast wave, is dependent on factors such as the standoff distance and the size of the explosive charge. When the distance from the detonation increases, the intensity of the blast pressure decreases, while the duration increases. The blast pressure can be categorised as either an incident blast pressure or a reflected blast pressure. The loading experienced by a structure is the reflected overpressure, i.e., the reflected blast pressure relative to the atmospheric pressure. The loading history typically consists of a positive overpressure phase and a negative overpressure phase, where the latter will have a lower intensity and often a longer duration. The positive overpressure phase can be described by the modified Friedlander equation [25], given by

$$P(t) = P_{\max}\left(1 - \frac{t}{t_{\mathrm{d+}}}\right)\exp\left(-b\frac{t}{t_{\mathrm{d+}}}\right) \tag{1}$$

where $P_{\max}$ is the maximum reflected overpressure, $t_{\mathrm{d+}}$ is the duration of the positive phase, and b is the decay coefficient used to describe the shape of the overpressure-time curve. Note that $t = 0$ refers to the arrival time of the blast wave. The negative phase is negligible compared to the positive phase in the experiments presented in this study. Thus, the modified Friedlander equation is sufficient to describe the blast loading on the laminated glass specimens. It should, however, be noted that the negative phase may have a pronounced effect on the blast response of glass plates (see, e.g., [26]).

3.2. Blast testing

The laminated glass was subjected to pressure loads generated by a shock tube, which is located at SIMLab at the Norwegian University of Science and Technology (NTNU). The produced loading history is similar to that of far-field explosions, and the shock tube is thus a safe alternative to explosive detonations [15]. Fig. 2 shows a sketch of the shock tube. It consists of a high-pressure chamber (the driver section), a firing section, a low-pressure chamber (the driven section), a window section, and a dump tank (with a volume of 5.1 m^3). The laminated glass specimen is attached to the end of the driven section which is positioned inside the dump tank. The pressure load is produced by built-up air pressure (in the driver section) that is sent down the driven section and transformed into a characteristic blast wave. When the blast wave reaches the test specimen, it is reflected and the pressure intensifies. The reflected overpressure represents the loading experienced by the laminated glass. We refer to the work by Aune et al. [15] for a detailed description and validation of the shock tube, and for the general experimental setup. The current blast tests were filmed by two synchronised high-speed cameras of type Phantom v1610 (with a recording rate of 24 kHz) or Phantom v2511 (with a recording rate of 37 kHz). The reflected overpressure is estimated by curve fitting the Friedlander equation (Eq. (1)) to data from two piezoelectric pressure sensors (denoted sensors 1 and 2 in Fig. 2). The sensors are placed 245 mm and 345 mm upstream the laminated glass specimen, and have a recording rate of 500 kHz. A validation of the curve-fitting procedure can be found in Aune et al. [15]. The validation was performed using a massive steel plate equipped with several pressure sensors. The Friedlander curve fit based on sensors 1 and 2 showed excellent agreement with pressure measurements directly on the massive steel plate. Note that, if the displacements of the specimen are large during loading,
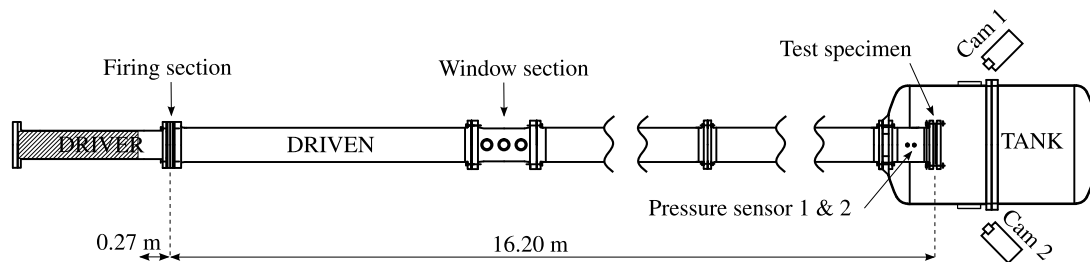

Fig. 2. Sketch of the shock tube seen from above [15].

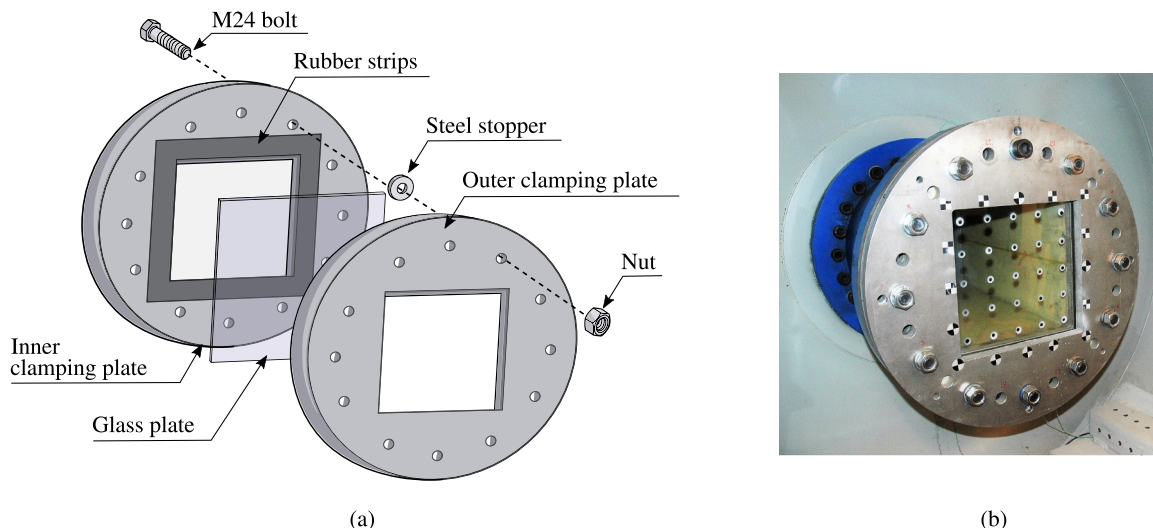(a)   (b)

Fig. 3. The custom-made fastening system for glass testing [13]: (a) disassembled, (b) assembled, showing the optical targets on the glass surface.

Table 2
Results from the blast tests on laminated glass for the five different classes of loads.

Test	P_{max} (kPa)	t_{d+} (ms)	b (-)	t_{frac} (ms)	D_{max} (mm)	i_+ (kPa·ms)	Comment
A-01	167.8	18.89	1.18	×	3.74	1109.3	No fracture
A-02	168.7	18.78	1.15	×	3.55	1117.9	No fracture
A-03	169.7	19.37	1.18	×	3.56	1150.3	No fracture
A-04	172.4	18.87	1.21	0.92	5.79	1129.2	Fracture in back plate
B-01	204.3	19.60	1.39	×	4.25	1324.5	No fracture
B-02	205.5	19.65	1.29	×	4.59	1371.7	No fracture
B-03	206.3	20.01	1.35	×	4.38	1379.9	No fracture
C-01	215.2	20.62	1.42	×	4.54	1456.2	No fracture
C-02	215.6	20.78	1.51	0.75	69.67	1462.8	Fracture in both plates
D-01	231.7	21.40	1.63	1.08	93.80[a]	1541.4	Fracture in both plates
D-02	237.4	20.23	1.44	0.63	95.41	1567.8	Fracture in both plates
D-03	237.7	21.09	1.48	0.75	121.61[a]	1619.5	Fracture in both plates
D-04	238.9	21.40	1.52	1.08	92.53	1634.6	Fracture in both plates
E-01	254.2	23.10	2.21	1.03	99.18	1674.5	Fracture in both plates
E-02	258.9	24.20	1.98	0.42	111.61[a]	1786.8	Fracture in both plates

[a] The middle optical target was no longer traceable after the specified D_{max}.

there may be an interaction between the specimen and the air, i.e., a fluid-structure interaction (FSI) effect. This interaction could cause a disagreement between the actual and the curve-fitted reflected overpressure. More details regarding the pressure measurements in the shock tube can be found in the work by Aune et al. [15].

Fig. 3 shows a custom-made fastening system for blast testing of glass specimens in the shock tube. The specimen is clamped between two 25 mm thick aluminium plates. Neoprene rubber strips (with a thickness of 4 mm, width of 50 mm, and a hardness of IRHD 50 ± 10) are glued to the clamping plates and hence positioned on each side of the glass. The inner clamping plate is placed closest to the driven section, and includes a 5.7 mm deep milled-out area to facilitate the setup. To properly fasten the outer clamping plate while limiting the clamping pressure on the glass, steel stoppers are placed on the bolts that connect the two clamping plates together. In total, twelve equidistant M24 bolts are used. The glass specimen has dimensions 400 mm × 400 mm, while the loaded area is 300 mm × 300 mm. For more details on the experimental setup, we refer to Osnes et al. [13].

To measure the deformation of the laminated glass and possible movements of the clamping plate during testing, we employed three-dimensional digital image correlation (3D-DIC). Checkerboard stickers with dimensions 12 mm × 12 mm were placed on the outer clamping plate, and 25 white circles with a central black dot, denoted optical targets, were spray-painted on the glass, see Fig. 3b. The distance between the circles was c/c 60 mm in both in-plane directions. A point-tracking procedure, available in the in-house 3D-DIC software eCorr [27], was used to track the optical targets and the checkerboard stickers

from the high-speed images of the tests. If a speckle pattern was painted on the laminated glass, we could have obtained the displacement field from 3D-DIC. However, this was not done, as it would reduce the visibility of fracture initiation and propagation in the glass plates during the tests. The point-tracking procedure was validated in Ref. [13].

3.3. Experimental results

Fifteen laminated glass specimens, consisting of two 3.8 mm thick glass plates and a 1.52 mm thick PVB interlayer, were tested. Table 2 presents results from these tests in terms of the maximum reflected overpressure P_{max}, Friedlander parameters t_{d+} and b, time of fracture initiation t_{frac}, maximum mid-point displacement D_{max}, and impulse of the positive pressure phase i_+. The table also includes a comment on whether fracture occurred in the glass plates or not. PVB fracture was not visible in any of the tests. The glass plate closest to the cameras, i.e., farthest away from the pressure load, is referred to as the back plate in this study. The maximum mid-point displacements were corrected for the average displacements of the outer clamping frame. This correction did not significantly alter the results since the average frame displacement never exceeded 0.2 mm.

The experimental programme is divided into five classes, denoted A, B, C, D and E, based on the intensity of the maximum reflected overpressure. The logging frequency of the high-speed cameras was 37 kHz for tests B-01, C-01 and E-01. For the remaining tests, the logging frequency was 24 kHz. The velocity of the shock wave was measured to be between 427 m/s and 463 m/s, resulting in a Mach number above 1 in
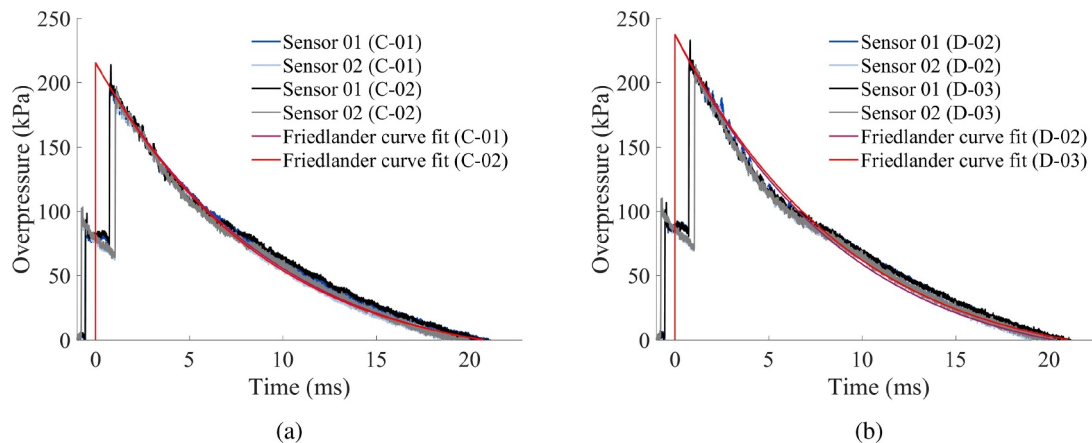
Fig. 4. Pressure measurements in sensors 1 and 2, including a representation of the reflected overpressure (Friedlander curve fit) for tests (a) C-01 and C-02, (b) D-02 and D-03.

all tests. These measurements were based on the recorded time used by the shock wave to travel between sensors 1 and 2, and the known distance between them. Examples of pressure data from the two sensors, including a Friedlander curve fit, are presented in Fig. 4. Note that the sensors are located some distance from the specimen, and therefore registers both the incident blast wave (at $t < 0$) and the reflected blast wave (at $t > 0$). The specimen is loaded by the reflected overpressure, represented by the fitted Friedlander curve. The results from Fig. 4

show that the pressure-time curves are highly similar despite the markedly different response of the plates within a class.

In tests D-01, D-03 and E-02, the mid-point optical target was no longer traceable after the specified D_{max} due to small glass fragments obstructing the visibility of the targets. Therefore, the true D_{max} might have been larger in these tests. The complete mid-point displacement versus time curves for all tests are displayed in Fig. 5. It is clear that the displacements are limited if fracture is not present in both glass plates.
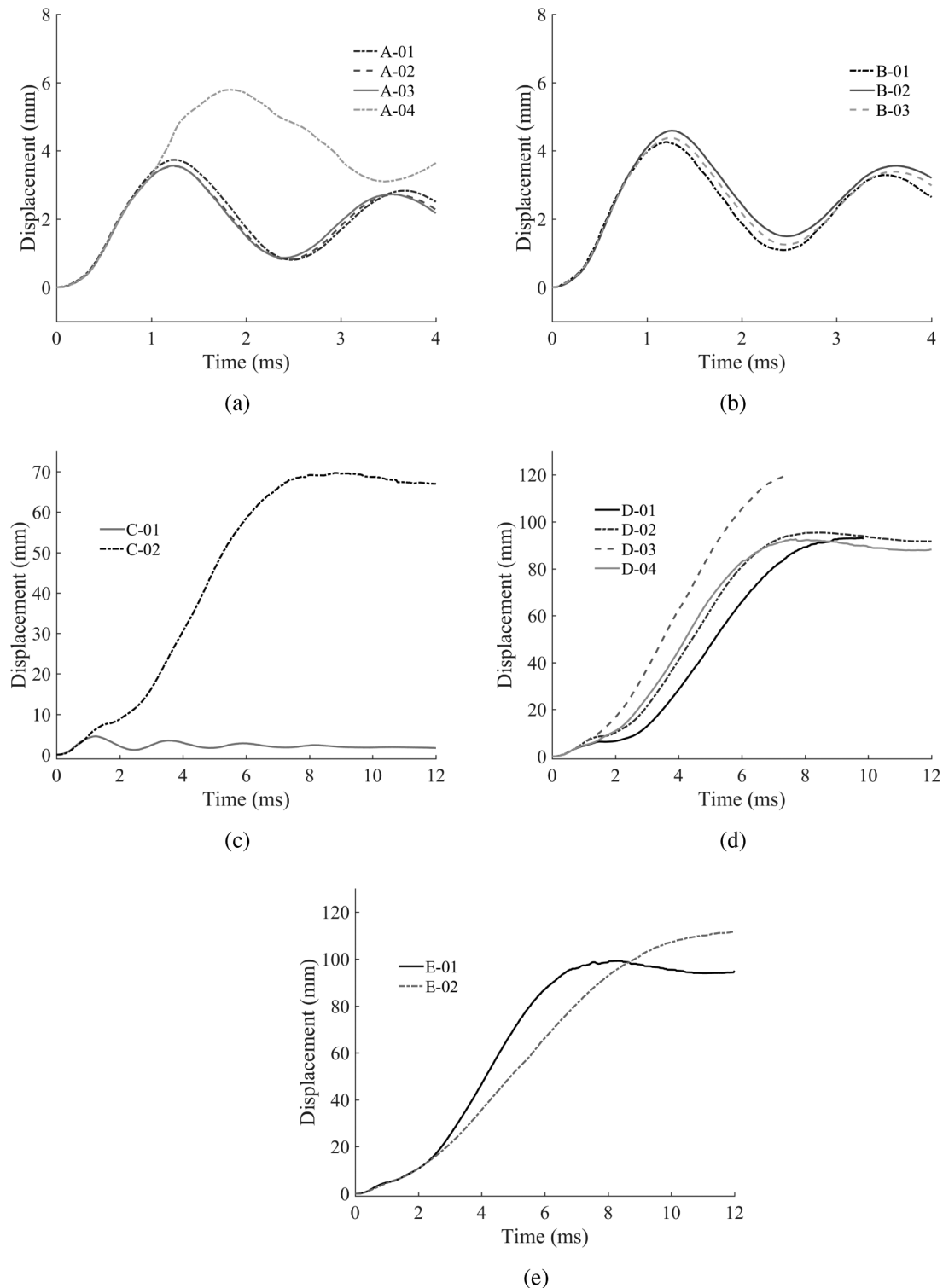

Fig. 5. Mid-point displacement versus time curves for all tests in class (a) A, (b) B, (c) C, (d) D and (e) E.
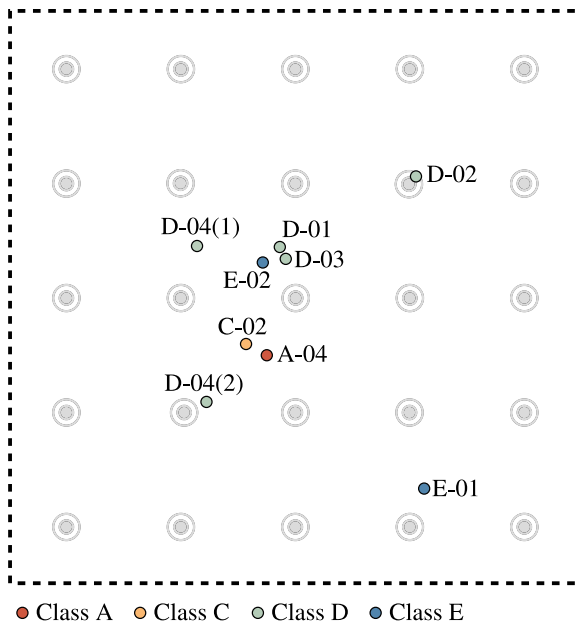
Fig. 6. Position of fracture initiation in the laminated glass based on all blast tests.

In test A-04, fracture occurred only in the back plate. This resulted in a different behaviour compared to the rest of the plates in class A for which no fracture occurred. Fig. 5 also illustrates that the displacements of the laminated glass specimens differ despite the pressure load being similar. This difference is caused by a variation in the position and time of fracture initiation in the tests. It seems that the fracture initiation governs a great deal of the subsequent behaviour of the laminated glass. When fracture is absent, the behaviour is similar. Furthermore, the tests depict the probabilistic fracture strength of glass. Fracture occurred (in the back plate) in one test of class A, but not for any of the tests of class B. In addition, fracture occurred (in both plates) for only one of the two tests of class C.

Fig. 6 shows the points of fracture initiation in the different tests. The dashed lines in the figure refer to the outer edges of the loading area, while the grey circles show the position of the optical targets. Note that for test D-04, fracture initiated at two different places at approximately the same time, referred to as (1) and (2). All fractures initiated in the back plate. The information from Table 2 and Figs. 5 and 6 suggest that a laminated glass displays a larger displacement when fracture initiates early and at the mid-point.

Detailed photo series from one of the high-speed cameras of tests A-04, C-02, D-03 and E-01 are presented in Figs. 7–10. As previously mentioned, only the back glass plate fractured in test A-04 (see Fig. 7). This implies that the PVB was not activated and therefore not allowed
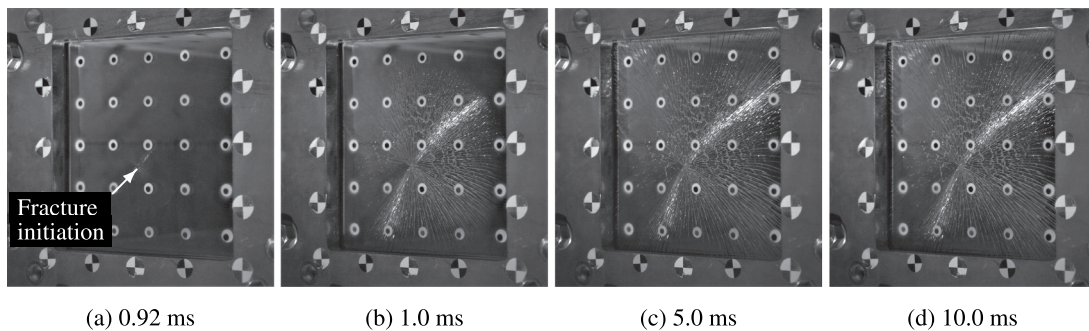

| (a) 0.92 ms | (b) 1.0 ms | (c) 5.0 ms | (d) 10.0 ms |

Fig. 7. Recorded photos in test A-04 captured at various points in time (see subcaptions).

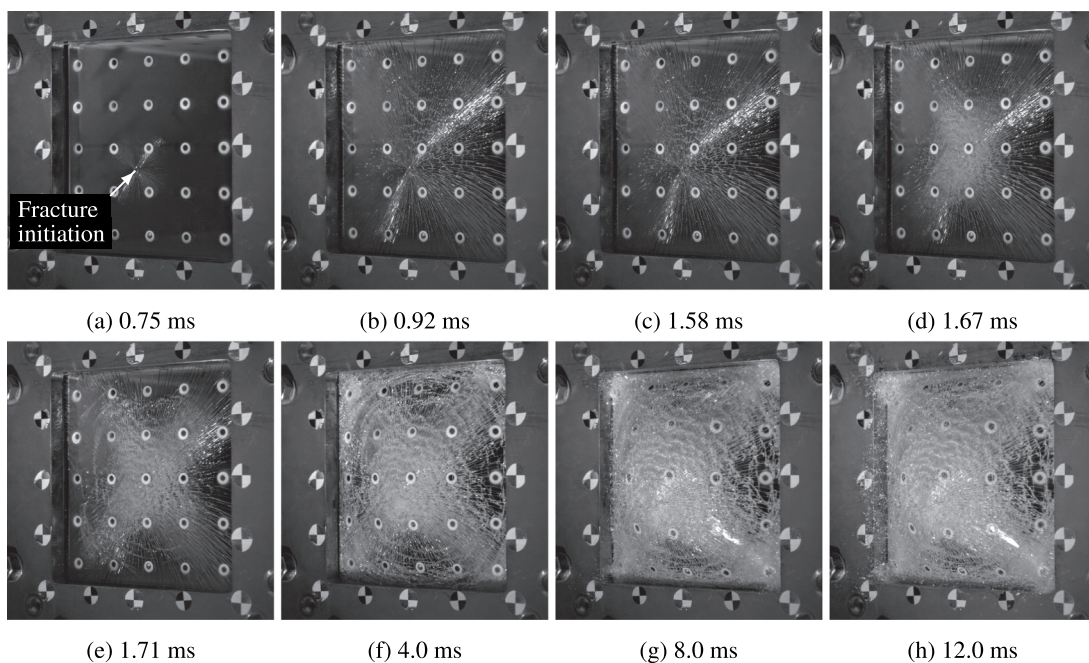| (a) 0.75 ms | (b) 0.92 ms | (c) 1.58 ms | (d) 1.67 ms |
| (e) 1.71 ms | (f) 4.0 ms | (g) 8.0 ms | (h) 12.0 ms |

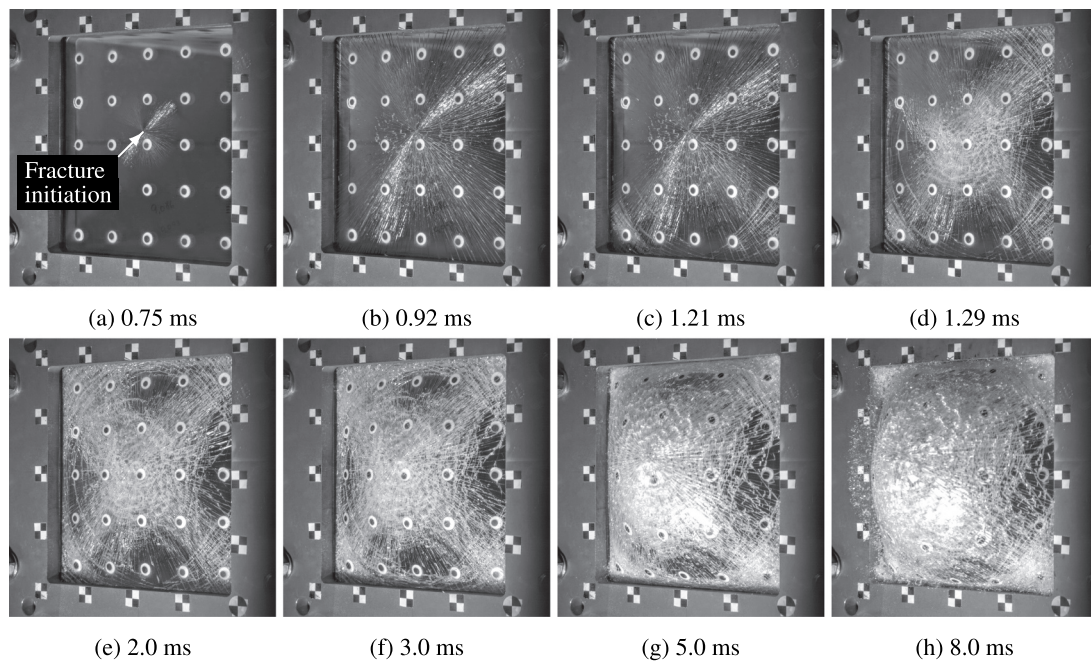Fig. 8. Recorded photos in test C-02 captured at various points in time (see subcaptions).

Fig. 9. Recorded photos in test D-03 captured at various points in time (see subcaptions).

to deform as a membrane. The glass fracture initiated close to the midpoint (a), and the cracks propagated towards the frame (b-c). Afterwards, there was no visible change in the appearance (d). In test C-02, both glass plates fractured and the PVB deformed significantly (see Fig. 8). Fracture initiated close to the mid-point of the back plate (a), with radial cracks propagating towards the edges (b-c). After some time, the front plate failed (d), and circumferential cracks formed in both glass plates (e-f). Towards the end of the test, nearly the entire plate was cracked into small pieces, owing to the significant deformation of the PVB. Delamination was also clearly visible (g-h). In test D-03, a slightly different sequence of events was obtained (see Fig. 9). As

in test C-02, fracture initiated close to the mid-point (a), with subsequent radial crack propagation (b). However, forming of circumferential cracks occurred earlier and closer to the corners (c-f). Delamination was also observed in this test (g-h). In test E-01 (Fig. 10), fracture initiation occurred far from the mid-point (a), giving a highly different fracture pattern than in tests C-02 and D-03, with non-radial cracks propagating from the initiation point (b-c). After some time the appearance was similar to tests C-02 and D-03, with fracture in the front plate (d), growth of circumferential cracks (e), cracking into small fragments in both glass plates (f), and subsequent delamination (g-h).
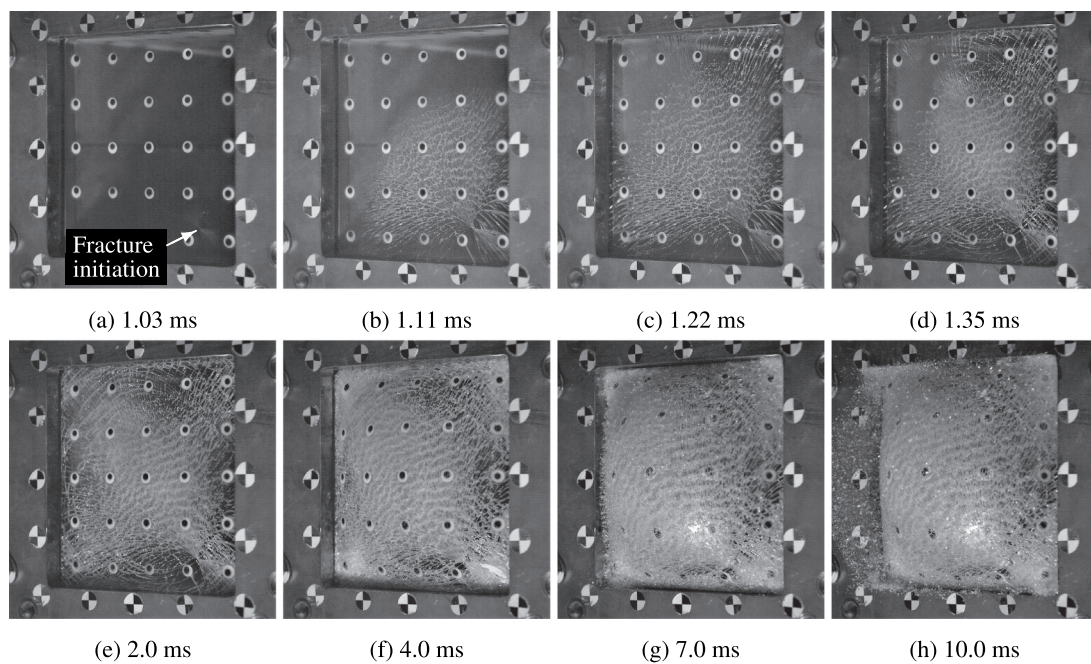

Fig. 10. Recorded photos in test E-01 captured at various points in time (see subcaptions).

4. Material modelling

4.1. Float glass

In this study, the float glass is modelled as a linear elastic material with a brittle failure criterion. The elastic behaviour is determined by Young's modulus E and Poisson's ratio ν given in Table 1. Fracture initiation occurs when a damage parameter D has evolved from 0 to 1 in an integration point, and is defined as

$$D = \frac{1}{t_s} \int_0^{t_s} H\left(\sigma_1 - \sigma_s\right)\left(\frac{\sigma_1}{\sigma_s}\right)^{\alpha_s} dt \tag{2}$$

where σ_1 is the major principal stress, σ_s the given stress threshold for fracture initiation, t_s is the fracture initiation time threshold and α_s is an exponent that controls the time to initiate fracture. The parameter t_s is introduced as a means to avoid that spurious peaks of stress result in fracture. Further, H is the Heaviside function, which ensures that damage does not evolve if σ_1 is less than σ_s. In regards to float glass, $D = 1$ generally corresponds to the growth of a pre-existing microscopic surface flaw into a macroscopic crack. The brittle failure criterion is motivated by the work of Tuler and Butcher [28].

When node splitting is applied, an initiated crack is made-up of new nodes and free element faces. Subsequently, propagation of a crack will occur if the stress intensity factor K_I in the integration points surrounding a crack tip reaches a critical value given by

$$K_I > K_{IC} \tag{3}$$

where K_{IC} is the fracture toughness for mode I loading. A crack tip is defined as a node that has not yet been split and belongs to at least one created element face. Note that the criterion given by Eq. (3) is only checked in the integration points closest to the crack in elements that are connected to a crack tip node. Based on the stress field in a linear elastic cracked body [29], the stress intensity factor K_I is calculated by

$$K_I = \alpha \sigma_1 \sqrt{\pi d} \tag{4}$$

where d is the distance from the integration points to the crack tip node and α is a constant determined by empirical calibration for the employed element type. The failure model is based on a deterministic approach, i.e., all glass elements are appointed the same fracture strength σ_s. Since the fracture strength of glass is known to be probabilistic [12], this will lead to a simplification of the glass failure modelling.

4.2. Polyvinyl butyral (PVB)

A viscoelastic material model, consisting of a hyperelastic spring in parallel with a nonlinear (viscous) dashpot, is used for the PVB material. The model employs a corotated formulation, i.e.,

$$\hat{\sigma} = \mathbf{R}^T \sigma \mathbf{R} \tag{5}$$

where $\hat{\sigma}$ is the corotated Cauchy stress tensor, σ is the Cauchy stress tensor, and $\mathbf{R}$ is the rotation tensor. The stress tensor $\hat{\sigma}$ is given by the sum of the stresses in the hyperelastic spring $\hat{\sigma}_A$ and the nonlinear dashpot $\hat{\sigma}_B$ as

$$\hat{\sigma} = \hat{\sigma}_A + \hat{\sigma}_B \tag{6}$$

The stress contribution $\hat{\sigma}_A$ is calculated as

$$\hat{\sigma}_A = \frac{\mu}{J\lambda_c^*} \frac{\mathcal{L}^{-1}(\lambda_c^*/\lambda_L)}{\mathcal{L}^{-1}(1/\lambda_L)} \mathbf{C}_{dev}^* + \frac{1}{J} K \ln(J)\mathbf{I} \tag{7}$$

where μ, λ_L and K are the initial shear modulus, locking stretch and bulk modulus, respectively. Further, $\mathcal{L}^{-1}$ is the inverse Langevin function, J is the Jacobian given by the determinant of the deformation gradient $\mathbf{F}$, and $\mathbf{I}$ is the identity tensor. The tensor $\mathbf{C}_{dev}^*$ is the deviatoric part of the isochoric right Cauchy-Green deformation tensor, and is defined as

$$\mathbf{C}_{dev}^* = \mathbf{C}^* - \frac{1}{3}\mathrm{tr}(\mathbf{C}^*)\mathbf{I}, \quad \mathbf{C}^* = J^{-2/3}\mathbf{C}, \quad \mathbf{C} = \mathbf{F}^T\mathbf{F} \tag{8}$$

Additionally, λ_c^* is an average chain stretch expressed as

$$\lambda_c^* = \sqrt{\frac{\mathrm{tr}(\mathbf{C}^*)}{3}} \tag{9}$$

The viscous stress contribution $\hat{\sigma}_B$ is calculated as

$$\hat{\sigma}_B = b_0(\lambda_c^* - 1)^{b_1}\left(\frac{\dot{\bar{\gamma}}_{dev}^{eff}}{\dot{\gamma}_0}\right)^{b_2}\left(\frac{\hat{\bar{\mathbf{D}}}_{dev}}{\dot{\bar{\gamma}}_{dev}^{eff}}\right) \tag{10}$$

where b_0, b_1, b_2 and $\dot{\gamma}_0$ are the viscous flow stress parameters, and $\dot{\bar{\gamma}}_{dev}^{eff}$ is an effective time-averaged deviatoric shear strain rate. The latter is defined as

$$\dot{\bar{\gamma}}_{dev}^{eff} = \sqrt{\frac{1}{3}\hat{\bar{\mathbf{D}}}_{dev} : \hat{\bar{\mathbf{D}}}_{dev}} \tag{11}$$

where $\hat{\bar{\mathbf{D}}}_{dev}$ is a time-averaged corotated deviatoric rate of deformation tensor calculated as

$$\hat{\bar{\mathbf{D}}}_{dev} = \frac{1}{c_{dec}} \int_0^t \hat{\mathbf{D}}_{dev} \exp\left(\frac{\tau - t}{c_{dec}}\right) d\tau \tag{12}$$

Here, c_{dec} is a viscous decay parameter and $\hat{\mathbf{D}}_{dev}$ is the corotated deviatoric rate of deformation tensor defined as

$$\hat{\mathbf{D}}_{dev} = \hat{\mathbf{D}} - \frac{1}{3}\mathrm{tr}(\hat{\mathbf{D}})\mathbf{I}, \quad \hat{\mathbf{D}} = \mathbf{R}^T\mathbf{D}\mathbf{R} \tag{13}$$

where $\mathbf{D}$ is the rate of deformation tensor. The presented model is motivated by a constitutive model by Bergström and Boyce [30]. In the original model, the viscous part is comprised of a Maxwell element instead of a single dashpot. By removing the spring in the Maxwell-element, the viscous stress is given explicitly; however, the need for numerical damping is introduced.

4.3. Adhesion and delamination

Adhesion between the PVB interlayer and the glass is modelled by merging the nodes in the PVB to the glass surface. Delamination, i.e., separation of the PVB nodes from the glass surface, can take place when the following criterion is reached.

$$\left(\frac{\max\{0, \sigma\}}{\sigma_{fail}}\right)^2 + \left(\frac{\tau}{\tau_{fail}}\right)^2 \geq \frac{1}{\xi^2} \tag{14}$$

Here, σ_{fail} is the tensile failure stress, τ_{fail} is the shear failure stress and ξ is a scale factor calculated as

$$\xi = \max(1, \sqrt{\Delta/\Delta_{ref}}) \tag{15}$$

where Δ is the local characteristic element size of the PVB and Δ_{ref} is the given element reference size. The scale factor ξ is included as a form of regularization, i.e., to account for a coarse mesh and its inability to generate possible stress concentrations. By including ξ, the stresses required to induce delamination is reduced if $\Delta > \Delta_{ref}$. Further, σ and τ are the normal and shear stresses calculated from the nodal forces at the PVB-glass interface. They are expressed as

$$\sigma = \mathbf{t} \cdot \mathbf{n}, \qquad \tau = \sqrt{\|\mathbf{t}\|^2 - \sigma^2} \tag{16}$$

where $\mathbf{t}$ is the surface traction and $\mathbf{n}$ is the node normal. After reaching the criterion defined by Eq. (14), a certain amount of energy must be consumed before delamination occurs. At this point, the stresses are equal to $\sigma = \sigma_{del}$ and $\tau = \tau_{del}$. Now, the stresses start to unload, following a linear function of the crack opening distance δ (along the direction given by $\mathbf{t}$). This relationship is illustrated in Fig. 11, and is given by
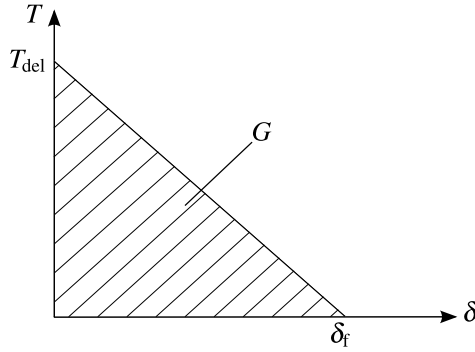
Fig. 11. Illustration of the stress unloading from reaching the criterion defined by Eq. (14).

$$
T = T_{\text{del}}\left(1 - \frac{\delta}{\delta_{\text{f}}}\right), \qquad T_{\text{del}} = \sqrt{\sigma_{\text{del}}^2 + \tau_{\text{del}}^2}
\tag{17}
$$

where T is the magnitude of the surface traction t, and T_{del} is T after reaching the criterion defined by Eq. (14). The crack opening distance when delamination occurs is δ_{f}. The consumed energy (over the crack area) is thus defined as

$$
G = \frac{1}{2}T_{\text{del}}\delta_{\text{f}} = \sqrt{\left(\frac{\sigma_{\text{del}}}{\sigma_{\text{fail}}}G_{\text{I}}\right)^2 + \left(\frac{\tau_{\text{del}}}{\tau_{\text{fail}}}G_{\text{II}}\right)^2}
\tag{18}
$$

where G_{I} and G_{II} are the given energy release per unit area for mode I and II loading. Note that the criterion is rate independent.

5. Finite element modelling

5.1. Finite element solver

In the current work, all numerical studies were carried out using the nonlinear explicit FE code IMPETUS Afea Solver [31]. The code is particularly suitable for simulations involving large deformations of structures and components under extreme loading conditions, due to the implementation of special features such as higher order elements and a node-splitting technique. Higher order elements provide additional robustness and accuracy, and can describe bending with only one element over the thickness, while node splitting enables modelling of fracture and crack propagation by separation of elements instead of deletion through element erosion. Node splitting involves generating new nodes and free element surfaces, and will occur when an integration point reaches a specified failure criterion. A crack will initiate at the nearest exterior node by splitting it into two nodes and separating neighbouring elements. After crack initiation, the software loops over all integration points surrounding the splitted node and calculates a stress (or strain) magnitude-weighted average direction of the major principal stress (or strain). Separation of elements (i.e., the crack) occurs in a direction as close as possible to the normal of the average major principal stress (or strain) direction [32]. In this study, the crack direction is chosen to be stress dependent. Holmen et al. [32,33] applied the 3D node splitting technique, in combination with higher order elements, in ballistic impact simulations of aluminum and steel plates. IMPETUS Afea Solver is compatible with graphic processing units (GPUs) for an increased computational speed, and version 4.0.2452 of the solver was used in this study.

5.2. Calibration of material model for PVB

The following calibration is based on a selection of uniaxial tensile tests on PVB dogbone specimens performed by Hooper et al. [22] and Del Linz et al. [24] (Fig. 1). The viscoelastic material model presented

Table 3
Fitted material parameters for the viscoelastic material model. >

K (MPa)	μ (MPa)	λ_L (-)	$\dot{\gamma}_0$ (s^{-1})	c_{dec} (s)	b_0 (MPa)	b_1 (-)	b_2 (-)
200	5	2	0.392	5×10^{-5}	11.54	0.152	0.197

in Section 4.2 was calibrated to the tensile test data by a combined curve-fitting and inverse-modelling approach. The fitted parameters are presented in Table 3. Simulations of the tensile tests were run to illustrate the agreement between the experiments and the calibrated model. The PVB specimen was modelled with symmetry along its length and width. One 27-node hexahedral element was used over the thickness since this is the element type that will be used in the blast simulations. Metallic grips were used to clamp the PVB to the testing machine in the experiments, and these were indirectly included by removing parts of the grip section in the model. Fig. 12 depicts the effective (von Mises) stress field in a simulation with a nominal strain rate of $400\,\text{s}^{-1}$ at three different levels of deformation (given by the logarithmic strain). The figure shows that the PVB specimen is able to deform greatly without necking, and that it has a close-to homogeneous stress field in the gauge area.

Fig. 13 displays the true stress versus logarithmic strain curves from the experiments and the simulations. Just like in the experiments, the true stress in the simulations was obtained from the reaction forces at the boundary of the specimen, and the logarithmic strain was found from the deformation of the gauge area. To investigate the versatility of the viscoelastic material model, we also simulated compressive Split Hopkinson Pressure Bar (SHPB) tests performed by Xu et al. [34]. The experiments were designed to minimise the friction between the bars and the PVB specimens, so we used a relatively low friction coefficient of 0.05 in our simulations. Fig. 14 compares the stress-strain curves from tests and simulations at three different strain rates. Note that the stress-strain data in Ref. [34] were given in terms of nominal values. The nominal stress and nominal strain in the simulations are calculated from the reaction force and displacement of the bars. As seen in the figure, the overall agreement between the simulation and experiment is good and deemed satisfactory for our purposes, despite some discrepancy at higher strains.

Note that the material tests were performed on PVB that was not treated in an autoclave. PVB is known to change from semitransparent to transparent after being subjected to heat and pressure, and one might therefore also expect some changes in the mechanical properties. This was shown in a study by Morison [35], where PVB specimens (both untreated and treated in an autoclave) were tested at four different loading rates. It was found that both the transition force (i.e., the force when the stiffness of the stress-strain curve changes) and the initial stiffness increased when the PVB was treated. This effect will be investigated numerically later on in the study.
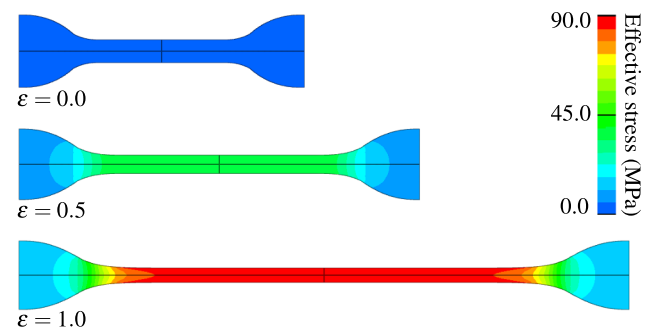

Fig. 12. Effective stress field in a simulation of a PVB tensile test with nominal strain rate of $400\,\text{s}^{-1}$ at three different levels of deformation.
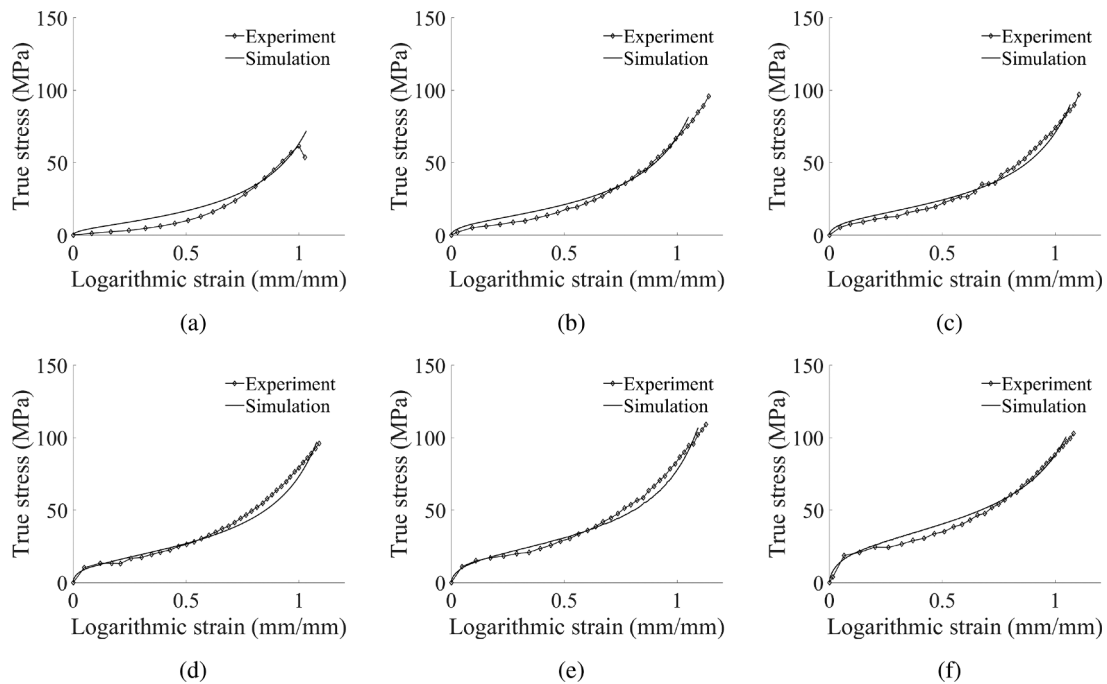
Fig. 13. True stress versus logarithmic strain curves from experimental tensile tests [22,24] and corresponding simulations with nominal strain rates: (a) 0.1 s^{-1}, (b) 2 s^{-1}, (c) 8 s^{-1}, (d) 20 s^{-1}, (e) 60 s^{-1} and (f) 400 s^{-1}.
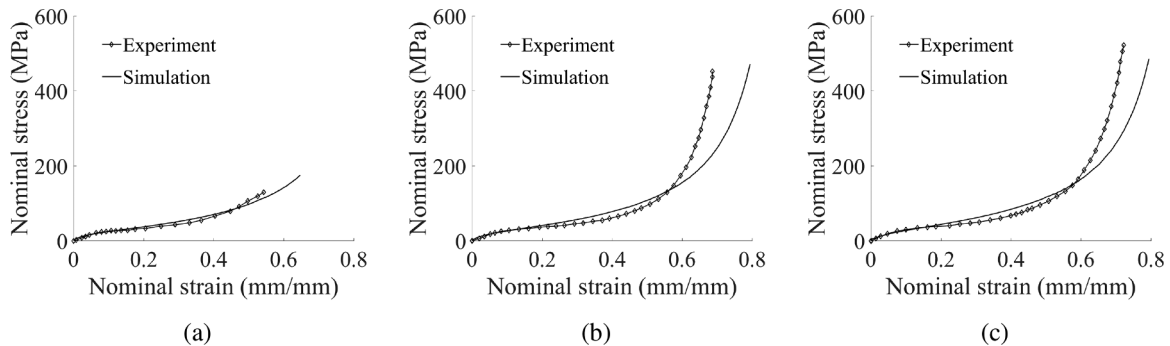

Fig. 14. Nominal stress versus strain curves from experimental compression tests [34] and corresponding simulations with nominal strain rates: (a) 700 s^{-1}, (b) 1200 s^{-1} and (c) 2200 s^{-1}.

5.3. Fracture stress of float glass

As mentioned in Section 4.1, the selected failure criterion for glass is based on a deterministic approach. Since the fracture strength of glass is probabilistic, this criterion represents a simplification. However, the approach was deemed satisfactory, as the main intention of the numerical study was to demonstrate the selected simulation techniques.

In the following two sections, we will present numerical studies on both monolithic (i.e., non-laminated) glass and laminated glass. The glass material is the same for both cases, i.e., 3.8 mm thick soda-lime silica float glass. For failure modelling of the glass plates, the fracture stress σ_s was chosen as 60 MPa and 90 MPa for the monolithic and laminated glass case, respectively. Two experimental tests were used to calibrate the failure criterion through an inverse modelling approach, which resulted in the two different values for σ_s. In the calibration process, we focused on a qualitative assessment of the simulation, in addition to the time of fracture initiation in the glass. The laminated glass case corresponds to test D-03. Details about the monolithic tests will be presented in the following section.

To justify the use of the values for σ_s, we carried out a statistical prediction of the fracture strength of the glass for the two cases. The analyses were done through the use of a stochastic strength model presented by Osnes et al. [13]. The input to the model is the stress field from an FE simulation of each of the two experimental tests. In these FE simulations, glass fracture is not included. The basis of the stochastic strength model is that fracture generally initiates in microscopic surface flaws under tensile loading. As a result, fracture depends on the applied normal stresses and the properties of the surface flaws. In the model, the information from the FE simulations is combined with an artificial flaw map, i.e., information about the location, size, and orientation of the flaws. The flaw map is varied over a number of iterations, i.e., virtual experiments. The stress intensity factor is evaluated and compared to the fracture toughness in every flaw within each iteration. The stochastic strength model outputs a prediction of the location and time of fracture initiation, and the probability distribution of the fracture load and fracture stress. More details regarding the stochastic strength model can be found in Ref. [13]. The number of employed iterations was set to 5000, and the calculation time was approximately 2 min for each of the two failure predictions. The statistical failure prediction that corresponds to the two experimental tests is presented in Fig. 15. According to the stochastic strength model, the failure stress for both the monolithic and the laminated glass test (D-03) is between ~ 55 MPa and ~ 120 MPa, see Fig. 15a. Therefore, the two values chosen for σ_s fall within the predicted values. Fig. 15b and c illustrates the predicted
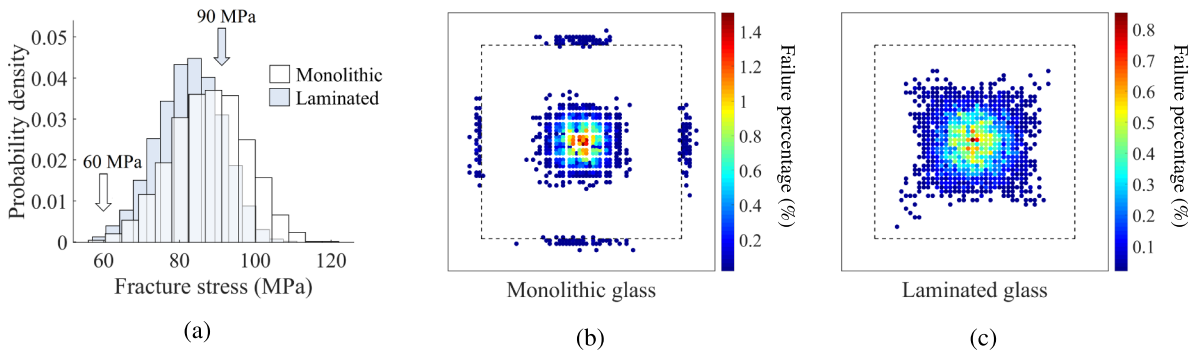
Fig. 15. Results from the stochastic strength model [13] in terms of (a) the probability density of fracture stresses, and the position of fracture initiation for (b) a monolithic glass and (c) a laminated glass (D-03).

position of fracture initiation, with the color bar representing the percentage of failure at the specific locations. It is seen that fracture initiation in the tests of class D falls within the predicted ones, see Figs. 6 and 15c.

5.4. Modelling of monolithic glass blast test

We chose to simulate the behaviour of monolithic float glass plates as an initial numerical study of the blast tests. To compare the simulations with representative test results, we used two experiments from an earlier study on blast-loaded monolithic glass that can be found in Ref. [13]. In the first experiment, no fracture was visible, while in the second experiment, fracture initiated close to the mid-point of the plate. The peak reflected overpressure P_{max} in the tests was 62.5 kPa for the unfractured plate and 63.7 kPa for the fractured plate.

The glass was modelled as linear elastic with the parameters presented in Table 1. The boundary conditions of the glass plate consisted of rubber strips with restriction in displacement at the outer surfaces, and four 5.7 mm thick rigid plates at the edges. The latter was included to mimic the milled-out area of the inner clamping plate. It was deemed unnecessary to include the entire clamping in the model since the rubber was glued to the clamping plates. Fig. 16a shows the FE model with the meshes of the different components. The rubber was modelled with 7 mm × 7 mm × 4 mm 64-node hexahedral elements, while for the glass we used 4 mm × 4 mm × 3.8 mm 40-node pentahedron elements. Pentahedron elements were chosen to allow crack growth to happen in several directions. The pressure loading is described by the Friedlander equation defined in Eq. (1), and the pressure was applied normal to the loading area of the glass. The Friedlander parameters t_{d+} and b were set to 11.82 ms and 0.73, respectively [13]. It should be

noted that we employ a purely Lagrangian (uncoupled) approach, and potential FSI effects are therefore neglected in this study. In other words, we assume that the pressure is unaltered by the deformation of the specimen. Generally, a coupled approach results in reduced deformations, in which the extent is dependent on the amount of FSI effects present [36].

The rubber material was modelled as linear elastic with a Young's modulus of 2 MPa, and a Poisson's ratio of 0.46 [13]. This results in a simplification of the material behaviour of the rubber, but it was proved sufficient to recreate the boundary conditions in the experiments. This is demonstrated in Fig. 17a, where displacements of the diagonal optical targets (denoted P0, P1 and P2 in Fig. 16b) in the simulation and the experiment of the unfractured glass plate are compared. The agreement between the simulation and the experiment is good. However, there is a small deviation during the spring-back of the plate (after around 3 ms), presumably due to the simplification of the rubber material model. Note that the displacements are taken from both sides of the symmetry lines, resulting in a total of nine points, see Fig. 16b. The displacements of points P0, P1 and P2 are as expected perfectly symmetric in the simulation of the unfractured plate, while some variation can be seen in the experiment.

In the simulation of the fractured plate, the fracture stress σ_s was set to 60 MPa (see Section 5.3), the fracture toughness K_{IC} to 0.75 MPa$\sqrt{m}$ (see Table 1), and the fracture initiation parameters t_s and α_s to 2× 10^{-7} s and 0.5, respectively. The parameters t_s and α_s were chosen as they resulted in a highly realistic fracture pattern. The displacements of points P0, P1 and P2 in both the experiment and simulation are presented in Fig. 17b. Note that the displacement in P2 was no longer traceable after about 4 ms, and is therefore not visible after this point. The response of the experiment and simulation is highly similar.
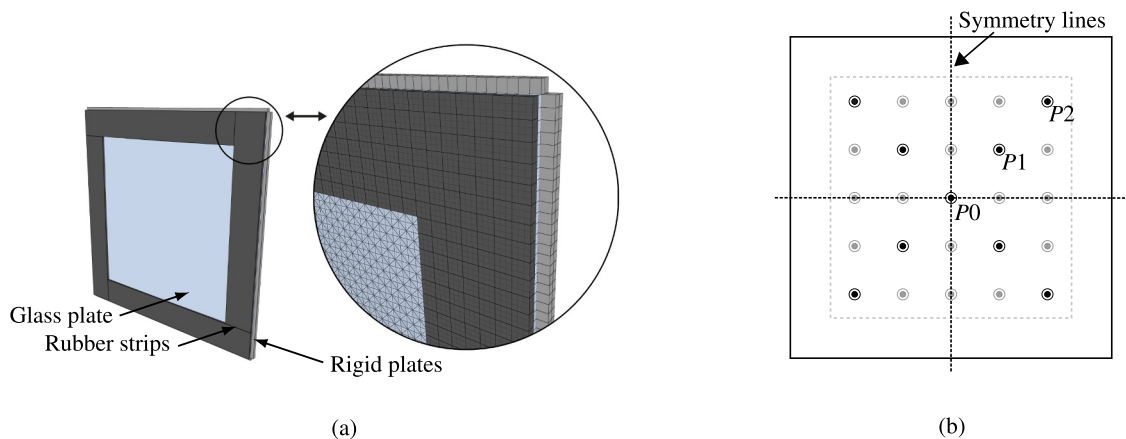

Fig. 16. FE model of the blast tests on monolithic float glass plates: (a) illustration of the mesh sizes, (b) points tracked in the FE model and the experiments, including symmetry lines.
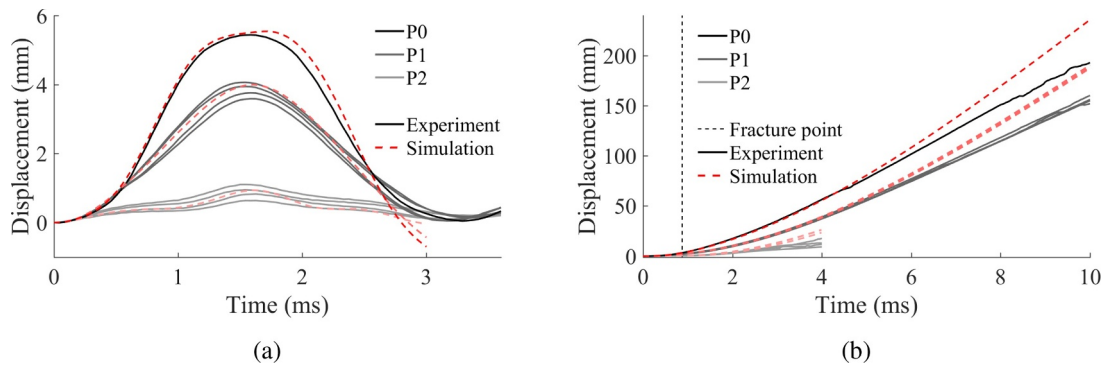
Fig. 17. Displacements of points P0, P1 and P2 versus time in experiment and simulation of (a) the unfractured plate and (b) the fractured monolithic glass plate [13].

However, some deviations are seen towards the end due to difference in position of fracture initiation and subsequent crack propagation in the glass. Fig. 18 compares pictures from the experiment and the simulation at three different stages throughout the test. The simulation captures many of the mechanisms seen in the experiment, including crack branching from the initiation point, formation of large glass splinters and free-flying fragments.

As previously mentioned, the employed fracture model is deterministic, which results in fracture initiation in the point of maximum major principal stress (i.e., in the mid-point of the glass plate). Since the glass plate in the experiment fractured close to the mid-point, it was possible to obtain a good agreement between the experiment and the corresponding simulation. In the aforementioned study on blast-loaded monolithic glass [13], fracture frequently initiated under the rubber strips. To obtain a comparable simulation for those tests, we would

have to include additional features such as distribution of initial damage to enable fracture initiation to happen away from the centre. Nevertheless, the presented simulation illustrates that node splitting enables a highly realistic description of the fracture and fragmentation in glass without loss of mass or momentum.

A small parametric study was carried out to investigate the sensitivity of the monolithic glass model. The study considered the glass mesh size, the fracture initiation parameters t_s and α_s, the fracture toughness K_{IC} and the fracture stress σ_s. Each parameter was given a lower and higher value compared to the base model. Additionally, a simulation with $\sigma_s = 90$ MPa was run, because this was the employed fracture stress for the laminated glass model, see Section 5.5. Fig. 19 presents a picture from each simulation (including the base model) at 5 ms after impact of the blast wave. The parametric study suggests that the brittle fracture criterion is most sensitive to the value of t_s, σ_s, and
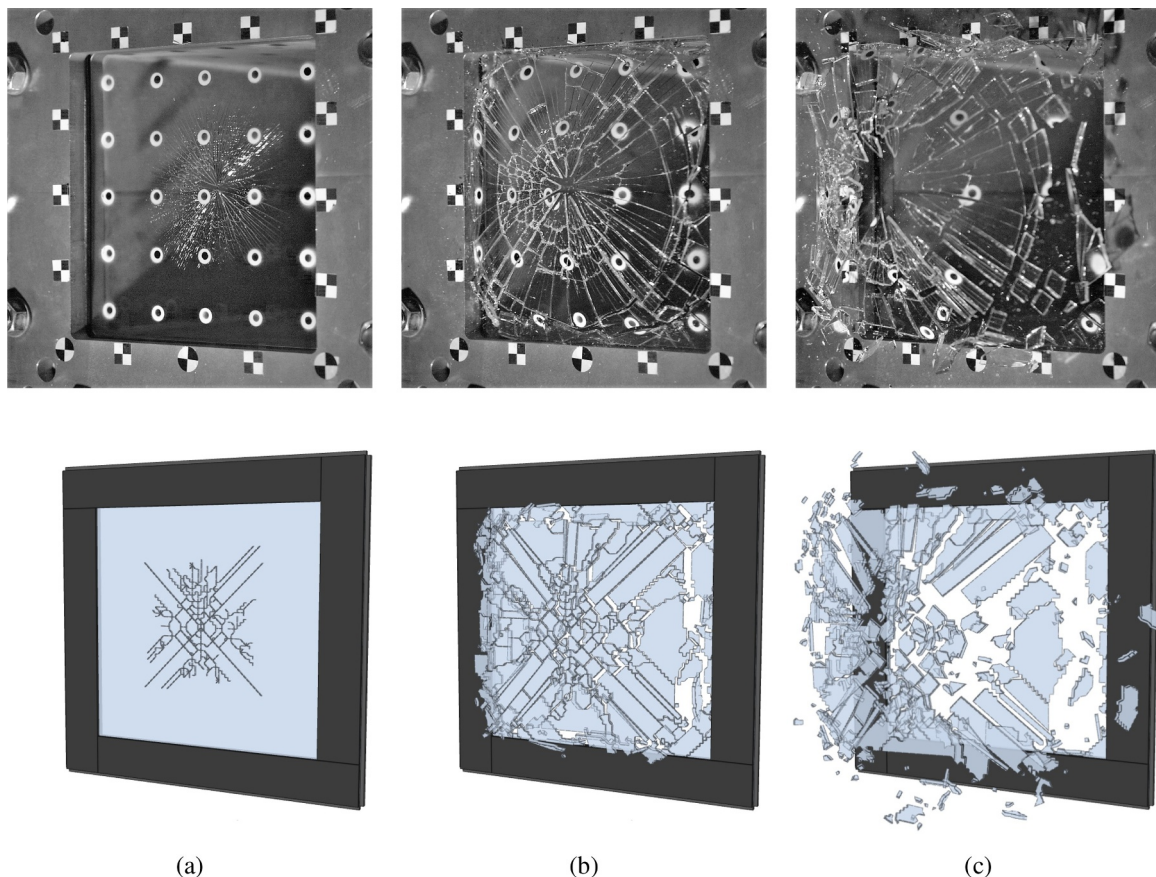

Fig. 18. Pictures of the fractured plate in the experiment and simulation at: (a) 0.9 ms, (b) 5 ms and (c) 10 ms.
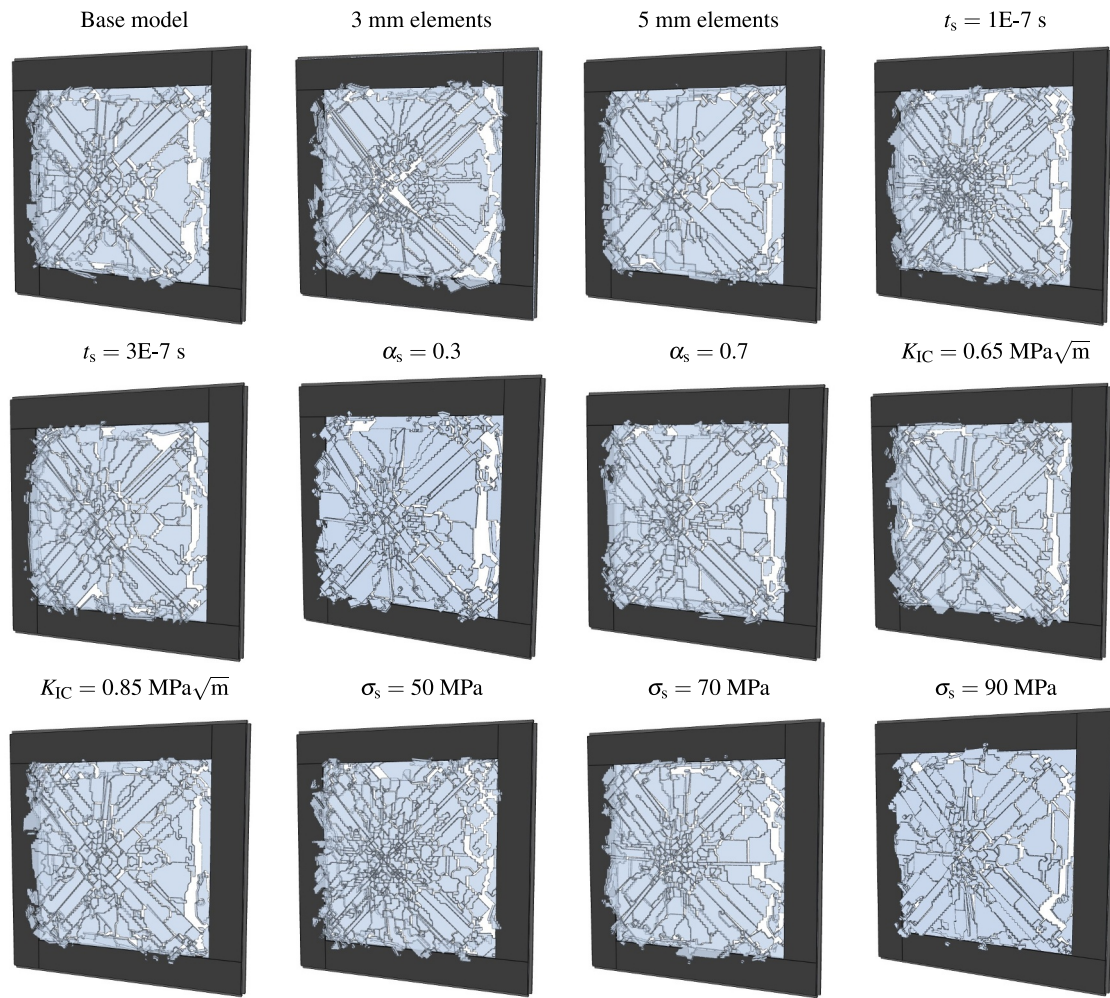
Fig. 19. Parametric study of blast-loaded monolithic glass. Pictures are taken at t = 5 ms. The base model utilised 4 mm elements and the parameters t_s= 2× 10^{-7} s, α_s= 0.5, K_{IC}= 0.75 MPa$\sqrt{m}$ and σ_s= 60 MPa.

the mesh size. The coarser mesh leads to fewer fragments, while a finer mesh gave an increased number of fragments, especially around the centre. The lower value of t_s also resulted in more fragments around the centre, not unlike the finer mesh model. This finding suggests that to get a similar cracking pattern for a finer mesh, one should increase the value of t_s. A fracture stress σ_s equal to 50 MPa gave excessive fracture over most of the plate, while σ_s equal to 70 MPa and 90 MPa gave similar results compared to the base model. The time of fracture

initiation naturally varied somewhat for the different values of σ_s.

5.5. Modelling of laminated glass blast tests

The numerical model of the laminated glass is similar to the monolithic glass model presented in Section 5.4. Differences include an increased fracture stress for the glass (σ_s = 90 MPa), and naturally, the additional glass and PVB layer with adhesion and a delamination
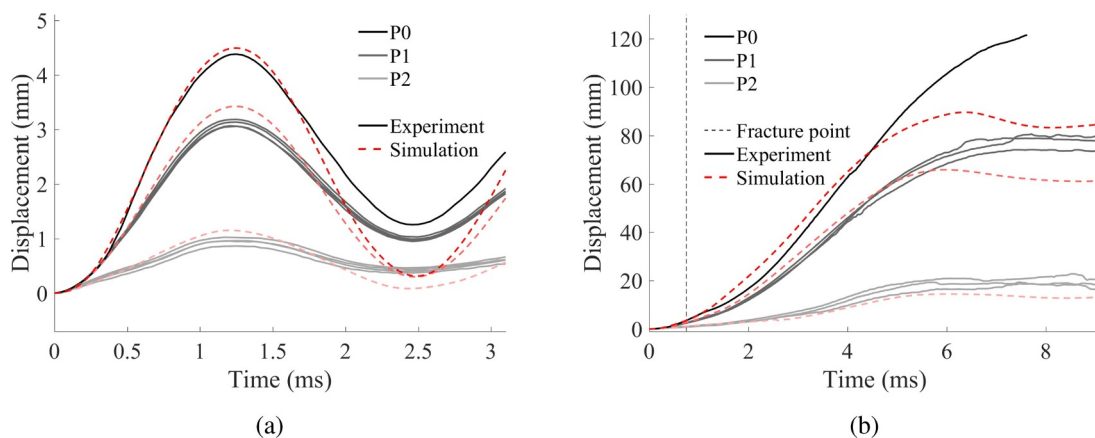

Fig. 20. Displacements of points P0, P1 and P2 versus time in experiment and simulation for test (a) B-03 and (b) D-03.

Table 4
The parameters of the delamination criterion.

| σ_{fail}	τ_{fail}	G_I	G_{II}	Δ_{ref}
12 MPa	10 MPa	1 N/mm	1 N/mm	2 mm

criterion. The loading was applied in the same manner as for the monolithic glass, but with the use of parameters from Table 2. We also chose to utilise the symmetry of the problem in these simulations to save computational time. Consequently, only one fourth of the experimental setup was modelled. The employed material model for the PVB with fitted parameters was presented in Section 5.2. The PVB layer was modelled with one 27-node hexahedral element over the thickness. The

pre-fracture behaviour of the laminated glass was examined first. We chose to model test B-03, and the resulting displacements of points P0, P1 and P2 in the experiment and corresponding simulation are presented in Fig. 20a. The simulation manages to recreate the overall experimental behaviour. However, just like in the unfractured monolithic glass simulation, there is some deviation during the spring-back of the plate (at around 2.5 ms). Still, the results indicate that the chosen PVB model and the fitted parameters are reasonable.

The parameters of the delamination criterion were chosen through a trial-and-error approach, and are presented in Table 4. These parameters lead to a realistic description of fracture and delamination, and are in the same range as parameters reported in studies of pre-cracked laminated glass specimens [9,10]. The chosen parameters did not lead to highly localised stretching of the PVB layer between glass elements,

(a) 0.75 ms   (b) 1.29 ms   (c) 2.0 ms   (d) 3.0 ms

(e) 4.0 ms   (f) 6.0 ms   (g) 8.0 ms   (h) 10.0 ms
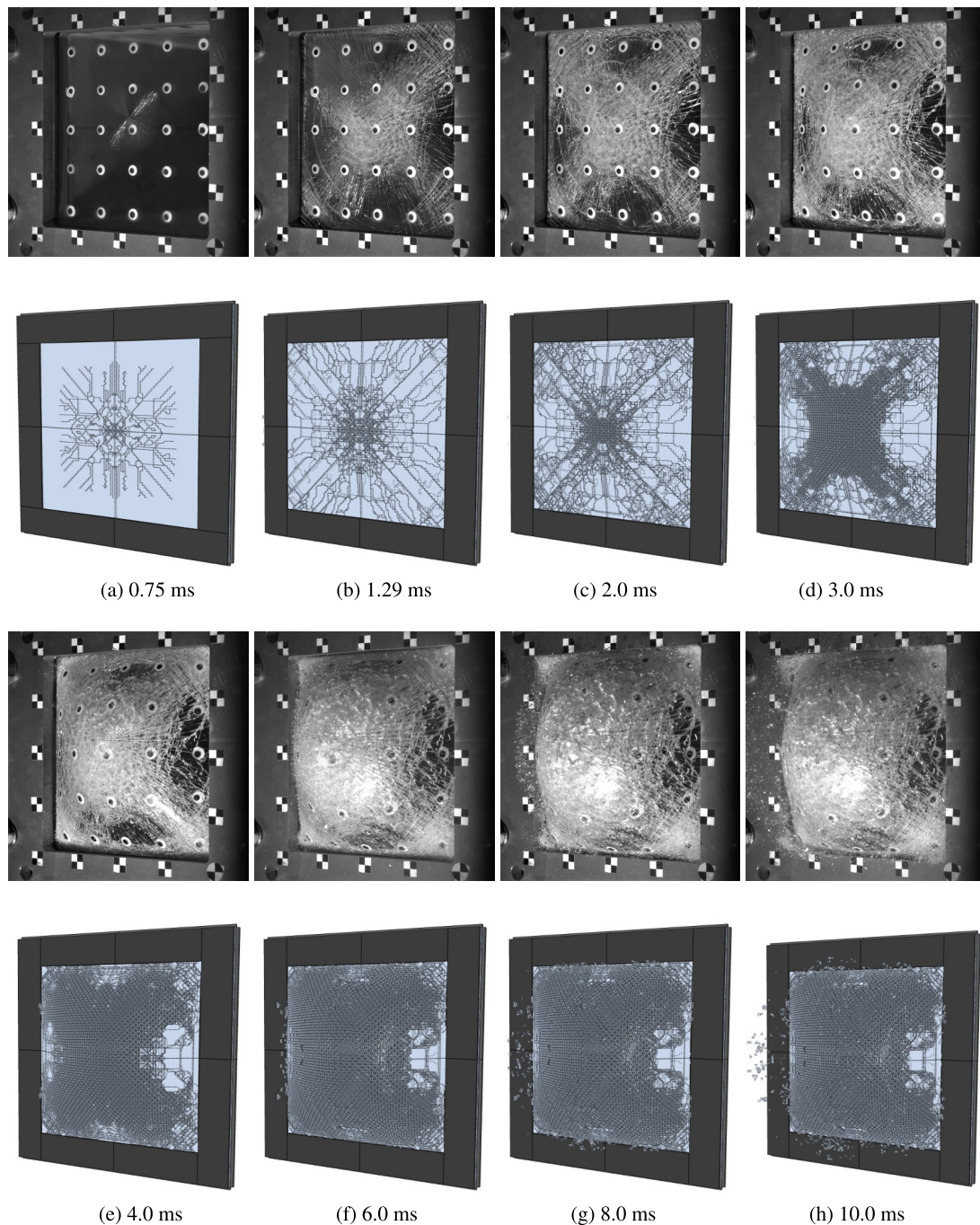
Fig. 21. Pictures of test D-03 and corresponding simulation at various points in time (see subcaptions).

14
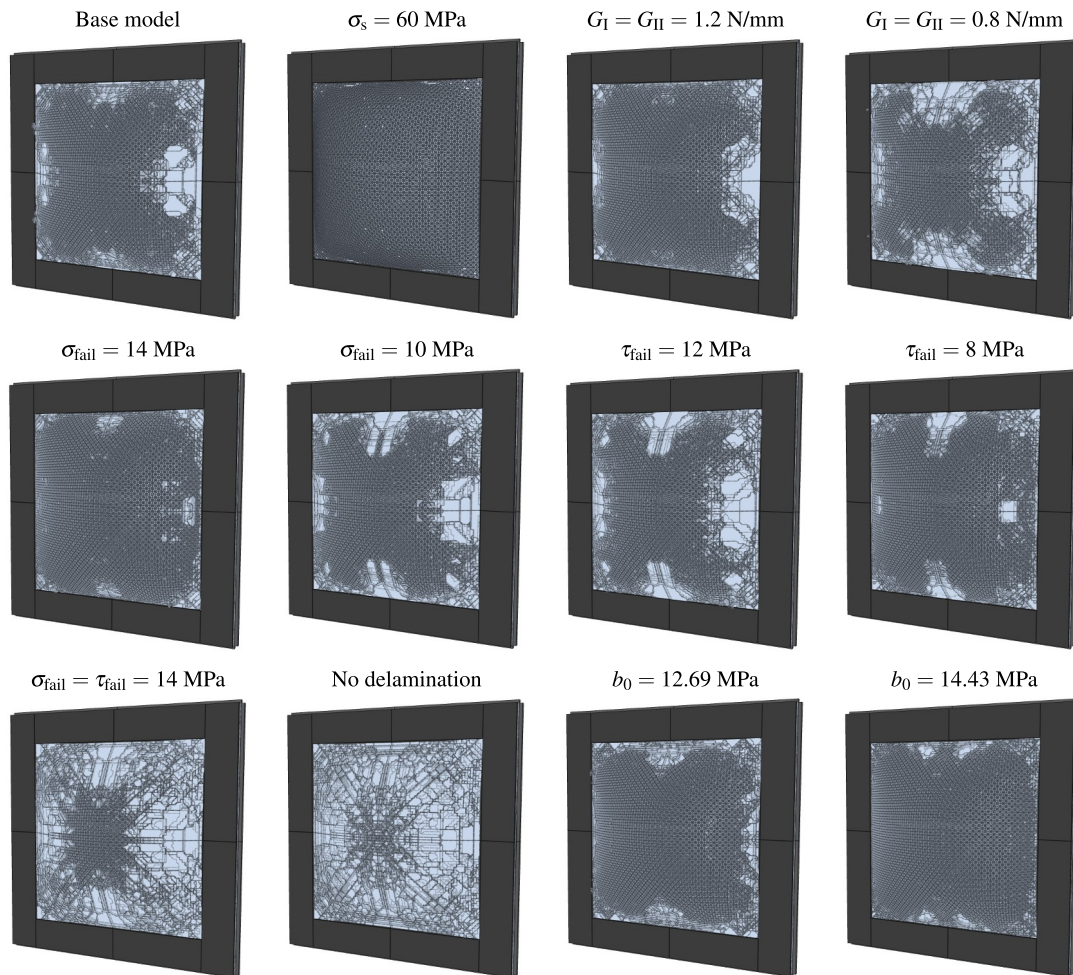
Fig. 22. Parametric study of blast-loaded laminated glass. The base model utilised the parameters σ_s= 90 MPa, σ_{fail}= 12 MPa, τ_{fail}= 10 MPa, $G_I = G_{II}$= 1 N/mm and b_0= 11.54 MPa. Pictures are taken at t = 4 ms.

which could be a problem with strong adhesion, i.e., delamination parameters that are too high. The element reference size Δ_{ref} was set to the same size as the PVB elements. Thus, according to Eq. (15), the scale factor ξ was equal to unity in these simulations.

For the simulation of a laminated glass that fractures, we chose to model test D-03, since fracture occurred close to the mid-point and delamination was observed in the test. Fig. 20b presents the displacements of points P0, P1 and P2 in the experiment and simulation. The behaviour is similar at the beginning, but deviates somewhat towards the end of the test. This result indicates that the cracking of the glass is more pronounced in the experiment than in the simulation, which leads to different levels of deformation in the PVB. Nevertheless, the displacements measured from the simulation follows the overall trend from the experiment, with a gradual increase from the start before it approaches a close-to constant value between 6 ms and 8 ms. Fig. 21 compares pictures from the experiment and the simulation at eight different points in time throughout the test. The simulation captures many of the mechanisms observed in the experiment, including fine cracking of the glass and detachment of glass fragments from the PVB. Additionally, the failure mode is highly comparable to the experiment, with extensive cracking in the centre and formation of diagonal cracks towards the boundary. Note that the back glass plate and the PVB are made partly transparent so that fracture in both glass plates is visible.

A parametric study was performed to investigate the sensitivity of

the laminated glass model. The study considered the delamination parameters σ_{fail}, τ_{fail}, G_I and G_{II}, and the viscous flow stress parameter b_0 in the PVB material model. The latter was included in an attempt to study the influence of the autoclave process on the laminated glass model. Increasing the value of b_0 leads to an increase in the transition force and the initial stiffness of the uniaxial stress-strain curve. This effect is observed experimentally for PVB after the autoclave process, as discussed in Section 5.2. In the current parametric study, we investigated the use of a higher and a lower value of the delamination parameters, in addition to excluding the delamination criterion altogether. For the viscous flow stress parameter b_0, two increased values were used. Additionally, a simulation with σ_s= 60 MPa was run, since this was the fracture stress we employed for the monolithic glass model in Section 5.4.

Fig. 22 presents pictures from each simulation (including the base model) at 4 ms after impact of the blast wave. We see that an increase in G_I and G_{II} leads to more cracking of the glass, whereas a decrease leads to less cracking. The response is reasonable because increased values of G_I and G_{II} imply that more energy has to be consumed before delamination can occur. This results in later and less delamination, which in turn requires the glass and the PVB to deform together. In this way, the glass fractures more extensively. Keep in mind that some delamination should be present to achieve a realistic fracture behaviour. If the delamination parameters σ_{fail} and τ_{fail} are increased excessively, or if no

delamination criterion is applied at all, the cracking of the glass becomes rather limited. With little delamination present, the glass fragments seem to prevent excessive deformation of the PVB, which reduces the cracking of the glass plates.

Furthermore, the parametric study suggests that mode II failure is dominating in terms of delamination. By increasing τ_{fail} alone, we are approaching the response with no delamination criterion. In other words, an increase in τ_{fail} leads to less delamination and less cracking of the glass. An equal change in σ_{fail} alone seems to have an opposite effect, as an increased value yields more cracking of the glass, whereas a decreased value results in less cracking. By increasing the value of b_0, the amount of cracking is increased, presumably as a result of a less flexible PVB and a decreased amount of delamination compared to the base model. For a reduction in the fracture stress, i.e., $\sigma_s = 60$ MPa, the glass plates undergo more cracking, which results from fracture initiation with subsequent fracture propagation at an earlier point compared to the base model. From the parametric study, it is evident that the behaviour of the laminated glass model is quite sensitive to all of the investigated parameters. It also appears that several combinations of the different parameters can result in a similar behaviour. It is therefore deemed necessary to investigate the input parameters in a more detailed manner in future studies, both through numerical simulations and experimental tests. Nevertheless, the numerical study reveals the potential of the selected numerical techniques.

6. Conclusions

In this study, we have investigated the possibility of simulating fracture and fragmentation of blast loaded laminated and monolithic (i.e., non-laminated) glass using explicit finite element analysis. In the simulations, we applied modelling techniques such as higher order elements and node splitting. The study also investigates the behaviour of blast-loaded laminated glass experimentally in a shock tube. In total, 15 laminated glass specimens, consisting of annealed float glass and PVB, were tested at five different pressure levels. The different tests displayed a variation in fracture initiation and subsequent post-fracture behaviour within the different pressure levels, demonstrating the stochastic fracture behaviour of glass.

The simulations of monolithic glass were able to capture behaviours such as crack branching from the fracture initiation point, formation of large glass splinters and free-flying glass fragments. We also conducted a parametric study to investigate the sensitivity of the FE model concerning the mesh density and the parameters in the failure criterion for glass. We observed that the model was most sensitive to the mesh density, the fracture stress σ_s and the fracture initiation parameter t_s. The simulations of the laminated glass were able to describe behaviours such as fine cracking of the glass plates, delamination between the glass and the PVB interlayer, and separation of glass elements from the interlayer. Just like in the monolithic glass simulations, a parametric study was carried out. In this case, we focused on the parameters of the delamination criterion. It was observed that the simulations were quite sensitive to all of the investigated parameters. Additionally, several effects that are known to be strain-rate sensitive (e.g., delamination and fracture toughness) were assumed rate independent in the FE model. Despite the fact that there are uncertainties linked to the selected method, the presented modelling techniques show great potential regarding simulations of blast-loaded glass. Finally, it is uncertain how the autoclave process on the laminated glass affects the PVB material. In the FE simulations of the laminated glass, we employed material tests of untreated PVB to calibrate the PVB material model. However, one might expect some change in the mechanical properties after this process. This effect should therefore be a topic of further investigation.

References

[1] Larcher M, Solomos G, Casadei F, Gebbeken N. Experimental and numerical investigations of laminated glass subjected to blast loading. Int J Impact Eng 2012;39(1):42–50.

[2] Hooper P, Sukhram R, Blackman B, Dear J. On the blast resistance of laminated glass. Int J Solids Struct 2012;49(6):899–918.

[3] Zhang X, Hao H. Experimental and numerical study of boundary and anchorage effect on laminated glass windows under blast loading. Eng Struct 2015;90:96–116.

[4] Zhang X, Hao H, Wang Z. Experimental study of laminated glass window responses under impulsive and blast loading. Int J Impact Eng 2015;78:1–19.

[5] Kumar P, Shukla A. Dynamic response of glass panels subjected to shock loading. J Non-Cryst Solids 2011;357(24):3917–23.

[6] Bermbach T, Teich M, Gebbeken N. Experimental investigation of energy dissipation mechanisms in laminated safety glass for combined blast-temperature loading scenarios. Glass Struct Eng 2016;1(1):331–50.

[7] Pelfrene J, Kuntsche J, Van Dam S, Van Paepegem W, Schneider J. Critical assessment of the post-breakage performance of blast loaded laminated glazing: experiments and simulations. Int J Impact Eng 2016;88:61–71.

[8] Osnes K, Dey S, Hopperstad O, Børvik T. On the dynamic response of laminated glass exposed to impact before blast loading. Exp Mech 2019. https://doi.org/10.1007/s11340-019-00496-1.

[9] Del Linz P, Hooper PA, Arora H, Wang Y, Smith D, Blackman BR, et al. Delamination properties of laminated glass windows subject to blast loading. Int J Impact Eng 2017;105:39–53.

[10] Franz J, Schneider J. Through-cracked-tensile tests with polyvinylbutyral (PVB) and different adhesion grades. Engineered transparency, international conference at glasstec, Düsseldorf, Germany. 2014. p. 135–42.

[11] Samieian MA, Cormie D, Smith D, Wholey W, Blackman BR, Dear JP, et al. Temperature effects on laminated glass at high rate. Int J Impact Eng 2018;111:177–86.

[12] Wachtman JB, Cannon WR, Matthewson MJ. Mechanical properties of ceramics. 2nd ed. John Wiley & Sons; 2009.

[13] Osnes K, Børvik T, Hopperstad OS. Testing and modelling of annealed float glass under quasi-static and dynamic loading. Eng Fract Mech 2018;201:107–29.

[14] Yankelevsky DZ. Strength prediction of annealed glass plates – a new model. Eng Struct 2014;79:244–55.

[15] Aune V, Fagerholt E, Langseth M, Børvik T. A shock tube facility to generate blast loading on structures. Int J Protect Struct 2016;7(3):340–66.

[16] NS-EN 572-1: Glass in building – Basic soda-lime silicate glass products – Part 1: Definitions and general physical and mechanical properties. Standard. CEN; 2012.

[17] Wiederhorn SM. Fracture surface energy of glass. J Am Ceram Soc 1969;52(2):99–105.

[18] Peroni M, Solomos G, Pizzinato V, Larcher M. Experimental investigation of high strain-rate behaviour of glass. Applied mechanics and materials. vol. 82. Trans Tech Publ; 2011. p. 63–8.

[19] Zhang X, Zou Y, Hao H, Li X, Ma G, Liu K. Laboratory test on dynamic material properties of annealed float glass. Int J Protect Struct 2012;3(4):407–30.

[20] Wiederhorn S, Bolz L. Stress corrosion and static fatigue of glass. J Am Ceram Soc 1970;53(10):543–8.

[21] Charles R. Static fatigue of glass: I & II. J Appl Phys 1958;29(11):1554–60.

[22] Hooper P, Blackman B, Dear J. The mechanical behaviour of poly (vinyl butyral) at different strain magnitudes and strain rates. J Mater Sci 2012;47(8):3564–76.

[23] Zhang X, Hao H, Shi Y, Cui J. The mechanical properties of polyvinyl butyral (PVB) at high strain rates. Constr Build Mater 2015;93:404–15.

[24] Del Linz P, Wang Y, Hooper P, Arora H, Smith D, Pascoe L, et al. Determining material response for polyvinyl butyral (pvb) in blast loading situations. Exp Mech 2016;56(9):1501–17.

[25] Cormie D, Mays G, Smith P. Blast effects on buildings. 2nd ed. Thomas Telford Publishing; 2009.

[26] Krauthammer T, Altenberg A. Negative phase blast effects on glass panels. Int J Impact Eng 2000;24(1):1–17.

[27] eCorr User Manual. Accessed: 2019-03-15. https://www.ntnu.edu/kt/ecorr.

[28] Tuler FR, Butcher BM. A criterion for the time dependence of dynamic fracture. Int

J Fract Mech 1968;4(4):431–7.

[29] Anderson TL. Fracture mechanics: fundamentals and applications. 3rd ed. 2005. p. 42. CRC press.

[30] Bergström J, Boyce M. Constitutive modeling of the time-dependent and cyclic loading of elastomers and application to soft biological tissues. Mech Mater 2001;33(9):523–30.

[31] IMPETUS Afea Solver. Accessed: 2019-03-18. http://www.impetus-afea.com/.

[32] Holmen JK, Johnsen J, Hopperstad O, Børvik T. Influence of fragmentation on the capacity of aluminum alloy plates subjected to ballistic impact. Eur J Mech A/Solids 2016;55:221–33.

[33] Holmen JK, Solberg JK, Hopperstad OS, Børvik T. Ballistic impact of layered and case-hardened steel plates. Int J Impact Eng 2017;110:4–14.

[34] Xu J, Li Y, Ge D, Liu B, Zhu M. Experimental investigation on constitutive behavior of PVB under impact loading. Int J Impact Eng 2011;38(2):106–14.

[35] Morison C. The resistance of laminated glass to blast pressure loading and the coefficients for single degree of freedom analysis of laminated glass. United Kingdom: Cranfield University; 2007. Ph.D. Thesis.

[36] Børvik T, Hanssen A, Langseth M, Olovsson L. Response of structures to planar blast loads–a finite element engineering approach. Comput Struct 2009;87(9–10):507–20.